View Online / Journal Homepage / Table of Contents for this issue
Dynamic Article Links

PCCP

Cite this: *Phys. Chem. Chem. Phys.*, 2011, **13**, 13096–13105

www.rsc.org/pccp

PAPER

Synthesis, surface morphology, and photoluminescence properties of anatase iron-doped titanium dioxide nano-crystalline films

Jinzhong Zhang, Xiangui Chen, Yude Shen, Yawei Li, Zhigao Hu* and Junhao Chu

Received 21st December 2010, Accepted 3rd May 2011
DOI: 10.1039/c0cp02924f

Published on 21 June 2011 on http://pubs.rsc.org | doi:10.1039/C0CP02924F
Downloaded by East China Normal University on 25 September 2012

Iron (Fe)-doped (0 to 4%) TiO_2 nano-crystalline (*nc*) films with the grain size of about 25 nm have been deposited on n-type Si (100) substrates by a facile nonhydrolytic sol–gel processing. X-ray diffraction measurements prove that the films are polycrystalline and present the pure anatase phase. X-ray photoelectron spectroscopy spectra indicate that the chemical valent state of Fe element is +3 and the Fe^{3+} ions replace the Ti^{4+} sites. The Fe dopant effects on the surface morphology, microstructure, and dielectric functions of the *nc*-Fe/TiO_2 films have been studied by atomic force microscope, ultraviolet Raman scattering and spectroscopic ellipsometry. With increasing Fe composition, the intensity of Raman-active mode B_{1g} increases, while that of the A_{1g} phonon mode decreases. The dielectric functions have been uniquely extracted by fitting ellipsometric spectra with the Adachi's dielectric function model and a four-phase layered model. It is found that the real part of dielectric functions in the transparent region and the optical band gap slightly decrease with the Fe composition due to the introduction of acceptor level Fe t_{2g}. Finally, the composition and temperature dependence of the surface and lattice defects in the Fe/TiO_2 films have been investigated by photoluminescence spectra in detail. At room temperature, the emission intensities decrease with increasing Fe compositions since the Fe incorporation could prolong the radiative lifetime and/or shorten the non-radiative lifetime. By analyzing the low temperature photoluminescence spectra, the intensities and positions of five emission peaks and shoulder structure can be unambiguously assigned. The phenomena could be reasonably explained by the physical mechanisms such as oxygen vacancies, localized excitons, self-trapped excitons, and indirect transitions, which are strongly related to the electronic band structure perturbed by the Fe doping.

1. Introduction

Among the metal-oxide nanostructures, nano-crystalline titanium dioxide (*nc*-TiO_2) has been widely investigated because of its unique physicochemical properties in photocatalysis, photoluminescence (PL), nonlinear optics, nanosensors, and so on.[1–3] Thus it has been used in the many fields related to photocatalysts, sensitized solar cells, optics, and chemical sensors.[4–7] As we know, TiO_2 exists naturally in three different crystalline polymorphs, *i.e.*, anatase, rutile, and brookite. Both anatase and rutile are tetragonal, whereas brookite is orthorhombic. It is well-known that the microstructure and surface defects of TiO_2 play a significant role in catalytic reactions, optical properties, and PL, *etc*. It has been well demonstrated that anatase is typically found to be more effective in photocatalytic and photovoltaic applications, while rutile is used for electronic and optical purposes due to its high dielectric constants.[8] In addition, the band gap of the anatase and rutile bulk phase is 3.2 eV and 3.0 eV, respectively. The primary structural difference between the two phases is the fact that the anatase phase is 9% less denser than the rutile phase, and has larger Ti–Ti distances, a narrower 3*d* band and a more pronounced localization of the Ti 3*d* states.[9] It is reported that the anatase TiO_2 film displays a visible luminescence band centered at about 505 nm (2.5 eV), which is ascribed to the oxygen vacancies, while a near-infrared luminescence band centered at about 835 nm (1.5 eV) in rutile TiO_2 is due to the intrinsic defects.[10] On the other hand, Lei *et al*. suggested that the visible broadband located at about 525 nm (2.4 eV) can be attributed to the F^+ center.[11] Thus, some further investigations are necessary to clarify the derivation of the visible PL bands for anatase TiO_2 material.

Since the discovery of ferromagnetism with Curie temperature above room temperature has been presented in Co-doped anatase TiO_2,[12] numerous theoretical and experimental investigations have been performed on the photocatalytic activity, PL properties, the related electronic properties of 3*d*

Key Laboratory of Polar Materials and Devices, Ministry of Education, Department of Electronic Engineering, East China Normal University, Shanghai 200241, People's Republic of China. E-mail: zghu@ee.ecnu.edu.cn; Fax: +86-21-54345119; Tel: +86-21-54345150

 This journal is © the Owner Societies 2011

Published on 21 June 2011 on http://pubs.rsc.org | doi:10.1039/C0CP02924F
Downloaded by East China Normal University on 25 September 2012

transition metal-doped TiO_2 for the last decades.[13–15] However, despite the remarkable attention on TiO_2-based oxides, the experimental results reported by different research groups on the origin of the PL properties have been controversial, especially for the visible luminescence emissions.[10,11] It is well-known that the physicochemical properties depend on the electronic band structure, which can be modified by different dopant elements, doping levels, fabrication technologies, and growth parameters, *etc*. Among all the dopants, iron (Fe) is frequently adopted because of its unique half filled-electronic structure. Recently, we reported the Fe doping effects on the dielectric constants and band gap for rutile TiO_2 films.[16] Nevertheless, the Fe energy level is still unresolved due to the absence of variable-temperature PL spectra. The Fe doping might narrow the band gap through the formation of a new intermediate energy level (Fe^{3+} t_{2g}), which is located at about 0.1 eV above the valence band of anatase TiO_2.[17] Thus, the visible-light photoactivity of TiO_2 will be enhanced by narrowing its band gap. In addition, Fe^{3+} ion can improve the photocatalytic activity of TiO_2 under the visible light irradiation, which is mainly due to the complexation of the hydroxyl groups bound to TiO_2 surface with the Fe ions.[13] Choi *et al.* reported that the substitution of Ti^{4+} ions in the TiO_2 lattice by Fe^{3+} ions was favored and the highest chloroform degradation efficiency under ultraviolet (UV) irradiation for the Fe^{3+} doped TiO_2 (0.5%) can be obtained.[18] It was found that the Fe-doped TiO_2 photocatalysts can absorb and utilize the visible light to photocatalyze the degradation of yellow dye.[19] Moreover, the N and Fe co-doped TiO_2 can improve the activity under both visible and UV light irradiation.[20] This indicates that the optical properties, especially luminescence, need systematic attention for Fe doped TiO_2 material with the anatase phase.

For several decades, the sol–gel technique has been extensively adopted to prepare many kinds of bulk and film materials owing to superiorities such as fast fabrication, composition control, large-area deposition and low cost.[21,22] However, it is difficult to obtain nanostructured TiO_2 films with a uniformly dispersed Fe replacement due to the fast hydrolysis and condensation rates *via* the traditional sol–gel/hydrolysis method, which results in lattice strain, expansion, and Ti deficiency.[23,24] In the present work, a facile non-hydrolytic sol–gel procedure was used to synthesize the homogeneous Fe-doped TiO_2 films with a variety of different Fe compositions (from 0 to 4%). This makes it possible to completely investigate the Fe doping effects on the surface/subsurface defects, optical and luminescence properties, which can provide an interesting insight on the surface states and energy levels from the Fe introduction. The factors influencing the surface morphology and optical properties and the probable mechanism of PL bands for anatase Fe/TiO_2 films have been investigated in detail.

2. Experimental

2.1 Chemicals

Analytical grade ethanol (C_2H_5OH, 99.7%) and acetate (CH_3COOH, 99.5%) were purchased from Shanghai Chemical Reagent Co., Ltd. Titanium butoxide ($Ti[O(CH_2)_3CH_3]_4$, 98.0%), acetyl acetone ($CH_3COCH_2COCH_3$, 99.0%), and ferric nitrate ninehydrate ($Fe(NO_3)_3{\cdot}9H_2O$, 98.5%) were purchased from Jiangsu YongHua Fine Chemical Reagent Co., Ltd. All the chemicals were used as received and without further purification. In addition, the n-type Si (100) wafers, whose electrical resistivity is 3 ± 1 Ω cm, were purchased from the Shanghai Guangwei Electronic Material Co., Ltd.

2.2 Synthesis of the (Ti, Fe)-precursor

The *nc*-Fe/TiO_2 films were deposited on n-type Si (100) substrates by a facile nonhydrolytic sol–gel method employing a spin-coating process. In order to obtain the effects of Fe composition on the morphology, optical constants and PL properties, the films were prepared in the Fe composition range of 0–4 mol%. Analytically titanium butoxide and pure ferric nitrate ninehydrate were used as the starting materials. As shown in Scheme 1, acetyl acetone and an equimolar amount of titanium butoxide were slowly added dropwise to the solution with a required volume ratio of $C_2H_5OH : CH_3COOH$ (16 : 1) under vigorous stirring at room temperature, respectively. Caution should be taken as the reaction is rather violent. Note that acetate and acetyl acetone were used here to adjust PH value and stabilize titanium butoxide, respectively. The Fe-doping with different compositions were achieved by dissolving a certain amount of ferric nitrate ninehydrate in the Ti-solutions. Then, the (Ti, Fe)-solutions were stired for 2 h at 50 °C to increase the homogeneity. The amount of Fe-doping was denoted as the fraction (%) number of Fe atoms to the sum of those of Ti and Fe atoms in the precursor solution.

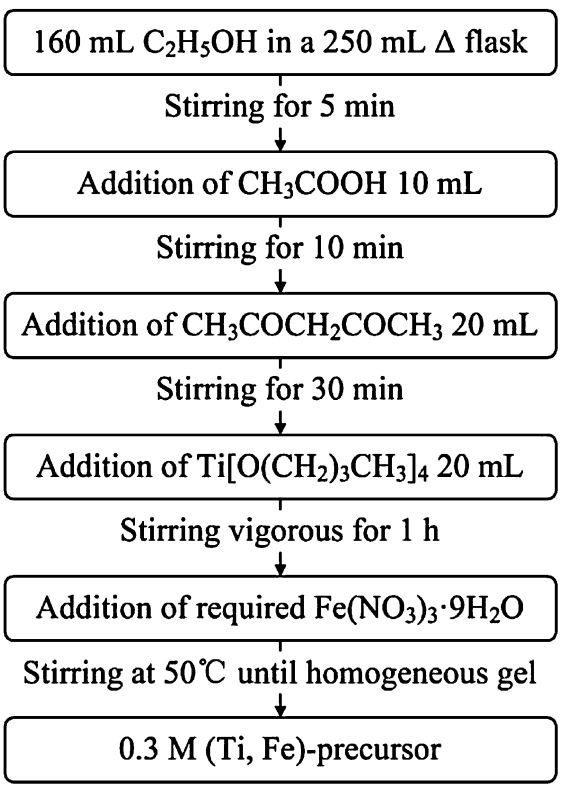

Scheme 1 Process of the preparation for pure and Fe-doped TiO_2 precursors.

Published on 21 June 2011 on http://pubs.rsc.org | doi:10.1039/C0CP02924F
Downloaded by East China Normal University on 25 September 2012

Finally, the 0.3 M precursor solutions were transparent without the precipitate phenomenon after two months. It should be emphasized that the deionized water, which quickly reacts with titanium butoxide, is not employed in the present method, as compared with the traditional hydrolysis method.[16,23]

2.3 Fabrication of *nc*-Fe/TiO_2 films

Before the deposition of (Ti, Fe)-precursor, n-type Si (100) substrates need to be cleaned in pure ethanol with an ultrasonic bath to remove physisorbed organic molecules from the surfaces, followed by rinsing several times with de-ionized water. Then the wafers were dried in a pure nitrogen stream before the deposition of the films. The Fe/TiO_2 films were deposited by spin coating of the 0.3 M (Ti, Fe)-precursor onto the substrates at the speed of 5000 rpm for 30 s. Each layer of the films was dried at 200 °C for 3 min, then pyrolyzed at 380 °C for 4 min to remove residual organic compounds, following annealed at 600 °C for 5 min in air ambient by a rapid thermal annealing procedure. The spin coating and annealing-treatment procedures were repeated many times to obtain the desired thickness. In addition, during the preparation of films in rapid thermal process, there are two main chemical reactions (hydroxylation and polycondensation), which are simply given as follows: $Ti[O(CH_2)_3CH_3]_4 + 4C_2H_5OH \xrightarrow{\Delta} Ti(OH)_4 + 4C_2H_5O(CH_2)_3CH_3$ and $nTi(OH)_4 \xrightarrow{\Delta} nTiO_2 + 2nH_2O$.

2.4 XRD, AFM, XPS, UV Raman, and SE

The crystalline structure of the *nc*-Fe/TiO_2 films was investigated by X-ray diffraction (XRD) using a Ni filtered Cu-Kα radiation operated at 40 kV and 200 mA (D/MAX-2550V, Rigaku Co.). In the measurement, a vertical goniometer (Model RINT2000) was used and continuous scanning mode (θ–2θ) was selected with a resolution of 0.02° and the 2θ range from 20 to 60°. The surface morphology was studied by atomic force microscopy (AFM) with the contacting mode in areas of 1 × 1 μm^2 (Digital Instruments Dimension 3100, Veeco). X-Ray photoelectron spectroscopy (XPS) measurements were carried out on a RBD upgraded PHI-5000C ESCA system (PerkinElmer) with Mg-Kα radiation ($h\nu$ = 1253.6 eV) and binding energies were calibrated by using the containment carbon (C 1s = 284.6 eV). Ultraviolet Raman experiments were done at room temperature by a micro-Raman spectrometer with a spectral resolution of 1.5 cm^{-1} (Jobin-Yvon LabRAM HR 800 UV). The ellipsometric spectra were recorded at room temperature by a near-infrared to ultraviolet (NIR-UV) spectroscopy ellipsometry (SE) in the wavelength range of 260–1700 nm (0.73–4.77 eV) with a spectral resolution of 2 nm (SC630UVN by Shanghai Sanco Instrument, Co., Ltd.). The incident angle of light was selected to 70° corresponding to the experimental optimization, which is close to the Brewster angle of the Si substrate.

2.5 Low-temperature PL characterization

The PL spectra in the photon energy range from 1.5 to 3.5 eV (350–830 nm) were collected by the same micro-Raman spectrometer with a charge-coupled device (CCD) detector and the laser source with the maximal excitation power of 30 mW. The films were set in an ultra-vacuum cavity during the low-temperature PL measurement and a close-cycled helium cryostat was used to provide continuous temperature in the range of 9–300 K (CCS-350, Janis Research Co.). Note that the 325 nm (3.82 eV) line of a He-Cd laser was applied as an excited source, which is much higher than the optical band gap of anatase TiO_2 films.

3. Results and discussion

3.1 Structure and surface morphology

The XRD patterns of the *nc*-Fe/TiO_2 films with different Fe compositions are shown in Fig. 1. It suggests that all the films are polycrystalline with a stronger (101) diffraction peak at about 25.4°. Besides the strong feature, there are some other weaker diffraction peaks (004), (200), (105). Note that no impurity phases (Fe_2O_3 and/or Fe_3O_4) are observed, which confirms that the films are of pure anatase structure. It indicates that the polycrystalline grains with different orientations are formed in the anatase films and the Fe atoms have been successfully incorporated into the host lattice. It should be emphasized that the standard error of all the peak positions in the XRD patterns is 0.01°. On the basis of the (200) and (004) diffraction peaks, the lattice constants $a = b$ and c of the Fe-doped TiO_2 films are estimated about 3.770 and 9.466 Å, respectively, which are slightly larger than the theoretical values of pure anatase ($a = b$ = 3.747 Å, c = 9.334 Å) due to the Fe substitution.[25] The differences of the lattice constants suggest that there are lattice distortions in the anatase films. As seen in Table 1, the average crystalline size r can be calculated to about 25 nm from the (101) diffraction peak according to the well-known Scherrer's equation. It should be emphasized that the grain size (about 21 nm) of *nc*-Fe/TiO_2 film with the maximum composition of 4% is the smallest due to the larger broadening at full width at half-maximum (FWHM).

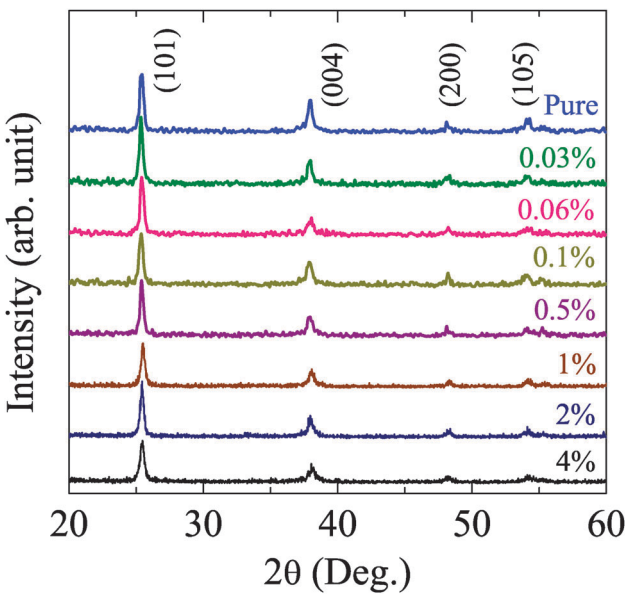

Fig. 1 The XRD patterns of the Fe/TiO_2 films grown on Si (100) substrates with the Fe compositions of 0, 0.03, 0.06, 0.1, 0.5, 1, 2, and 4%, respectively.

This journal is © the Owner Societies 2011

Table 1 The peak positions and FWHM of diffraction peaks for anatase Fe/TiO_2 films with the Fe compositions (C_{Fe}) determined from the XRD patterns in Fig. 1

Samples	C_{Fe}		Peak positions (°)			FWHM (°)	Lattice constants		Grain size
Fe/TiO_2	%[a]	%[b]	(101)	(004)	(200)	β(101)	$a = b$/Å	c/Å	r (nm)
A	0	—[c]	25.40	37.95	48.18	0.37	3.774	9.477	24
B	0.03	—	25.36	37.92	48.18	0.37	3.774	9.483	25
C	0.06	—	25.43	37.97	48.22	0.37	3.771	9.472	25
D	0.1	—	25.36	37.90	48.22	0.38	3.771	9.489	24
E	0.5	0.3	25.41	37.94	48.17	0.35	3.775	9.478	26
F	1	0.5	25.51	38.06	48.32	0.38	3.764	9.451	24
G	2	1.9	25.43	38.00	48.27	0.36	3.768	9.465	25
H	4	3.8	25.44	38.09	48.21	0.42	3.772	9.442	21

[a] The nominal atomic composition. [b] The atomic composition is derived by the XPS spectra. [c] The signal "—" means that the composition is below the instrument detection limitation.

Published on 21 June 2011 on http://pubs.rsc.org | doi:10.1039/C0CP02924F
Downloaded by East China Normal University on 25 September 2012

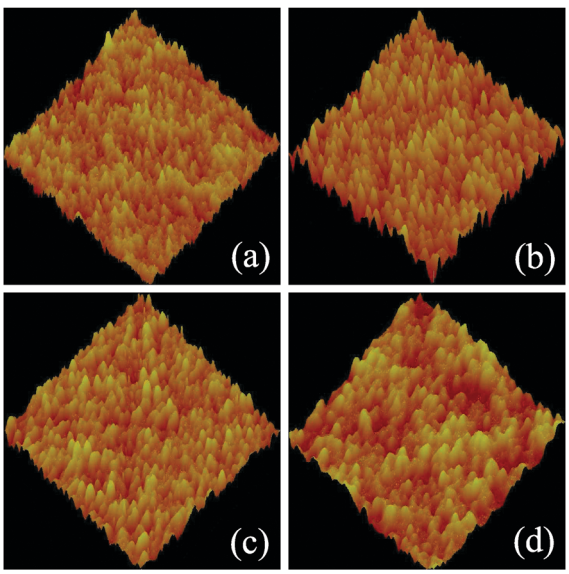

Fig. 2 AFM three-dimensional images of the *nc*-Fe/TiO_2 films with the Fe compositions of (a) 0%, (b) 0.1%, (c) 0.5%, and (d) 4%, respectively. Note that the scale height is 5 nm and the measured area is 1 × 1 μm^2.

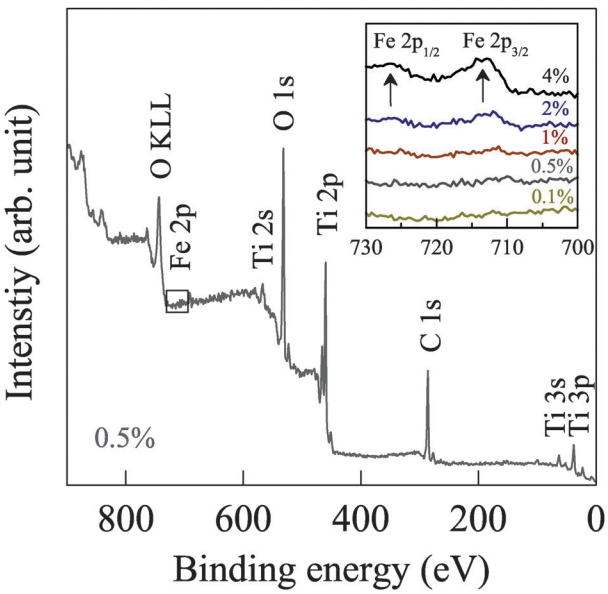

Fig. 3 Overall core level XPS spectra for the Fe/TiO_2 film with the nominal Fe composition of 0.5%. The Fe $2p_{1/2}$ and $2p_{3/2}$ spectra for the *nc*-Fe/TiO_2 films with the Fe composition rang of 0.5–4% is enlarged in the inset, which is illustrated by the symbol square (□) in the overall core level XPS spectra.

Furthermore, it has been reported that the addition of Fe element results in the slower crystallization rate for the Fe/TiO_2 films.[26] On the other hand, Fig. 2 shows the AFM three-dimensional images of the Fe/TiO_2 films and the root-mean-square value of the surface morphology is from 0.6 to 1.1 nm with the Fe dopant. It suggests that the surface becomes much rougher with increasing Fe composition. When compared with the rutile Fe-doped TiO_2 films, however, the surface of the present Fe/TiO_2 films is smoother due to the larger thickness value. The remarkable variation can obviously effect the optical properties and surface oxygen vacancies of the films such as dielectric constants, optical band gap, PL properties, and surface states discussed in the following.

3.2 XPS of the *nc*-Fe/TiO_2 films

As an example, Fig. 3 shows the overall core level XPS survey spectra of Fe-doped TiO_2 films with the composition of 0.5%. The XPS peaks show that the Fe/TiO_2 films contain Ti, O, and Fe elements. Furthermore, the Ti 2p, O 1s, and C 1s are located at about 460, 531, and 286 eV, respectively. Note that the binding energy of Ti is higher than that in bulk TiO_2 (459 eV), which may be attributed to the formation of vacancies in the present films.[17] In order to check if there are iron and/or iron oxide species such as metallic Fe, FeO, Fe_3O_4, and Fe_2O_3 and analyze the chemical bonding states in these samples, the Fe 2p core-level XPS spectra are shown in the inset of the Fig. 3. It illustrates that the binding energy of Fe $2p_{3/2}$ is located at 713.5 eV, which is significantly different from those of metallic Fe (706.8 eV), FeO (709.5 eV), Fe_3O_4 (710.4 eV), and Fe_2O_3 (710.6 eV), which excludes the possibility of the iron oxide cluster formations.[27] The XPS results indicate that the chemical valent state of Fe is +3 and the Fe^{3+} ions replace the Ti^{4+} ones, which agrees with the result from the XRD analysis. Normally, the XPS technique can identify all elements, whose concentration is above the detection limitation of 0.1%, except for H and He. Therefore, there is no resolving trace of the Fe element when the composition of the

Published on 21 June 2011 on http://pubs.rsc.org | doi:10.1039/C0CP02924F
Downloaded by East China Normal University on 25 September 2012

Fe/TiO_2 films is smaller than 0.5%. As can be seen in Table 1, the real amount of the doped Fe element in the Fe/TiO_2 films is 0.3, 0.5, 1.9, and 3.8%, which is in good agreement with the nominal atomic compositions of 0.5, 1, 2, and 4%, respectively.

3.3 Raman scattering of the *nc*-Fe/TiO_2 films

The crystallographic structure of anatase TiO_2 is tetragonal with the space group D_{4h}^{19} ($I4_1/amd$) and the primitive cell contains two formula units per unit cell and shows six first-order Raman-active modes ($A_{1g} + 2B_{1g} + 3E_g$) at the Γ point of the Brillouin zone.[28,29] According to the Perdew-Burke-Ernzerbof (PBE) functional, Kamisaka *et al.* reported that the theoretical Raman frequency of E_g, E_g, B_{1g}, B_{1g}, A_{1g}, and E_g is located at 128, 158, 388, 514, 521, and 638 cm^{-1}, respectively.[30] The $2E_g$ modes occurring at lower frequencies (<300 cm^{-1}) can not be observed due to the experimental limitation in the present work. The other four Raman-active phonon modes of anatase Fe/TiO_2 films with different Fe compositions are shown in Fig. 4. In addition, there is a second-order Raman scattering feature located at about 685 cm^{-1}, which appears with a shoulder structure. As compared with the rutile Fe-doped TiO_2 films,[16] it further confirms that the Fe/TiO_2 films are of the pure anatase phase and no rutile or brookite impurity can be detected. The four phonon modes of anatase TiO_2 are found at about 393, 515, and 632 cm^{-1} (superimposed with the 515 cm^{-1} band), which are assigned to the Raman-active modes of anatase phase with the symmetries of B_{1g}, $B_{1g} + A_{1g}$, and E_g, respectively. The peak positions and intensities of the above phonon modes are in good agreement with the experimental data reported for the pure anatase compound.[31] Note that the B_{1g} and A_{1g} phonon frequencies are too close to be distinguished.

In order to further study the lattice vibrations and microstructure, Fig. 5 presents a five-peak fit of the Raman spectra

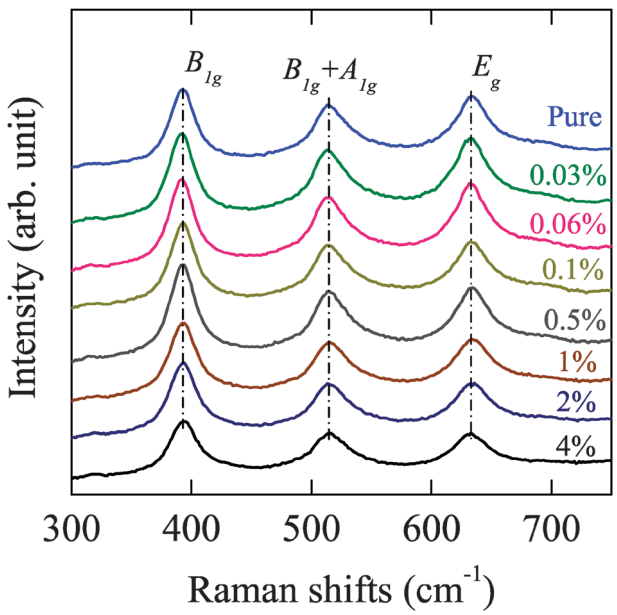

Fig. 4 The Raman spectra of the Fe/TiO_2 films with different Fe compositions under the excitation line of 325 nm. The dashed lines show the fundamental phonon mode frequency.

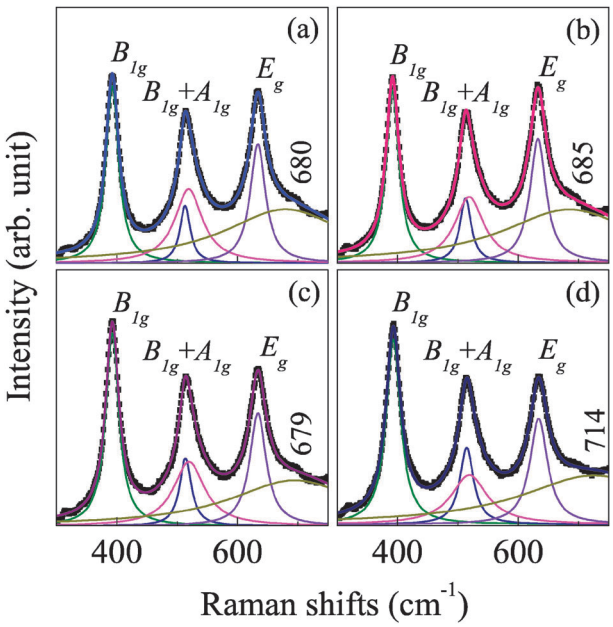

Fig. 5 A five-peak fit of the Raman spectra for the Fe/TiO_2 films with the compositions of (a) 0%, (b) 0.06%, (c) 1%, and (d) 4%, respectively. The four first-order and one second-order Raman phonon modes are indicated.

recorded in the range of 300–750 cm^{-1} for the *nc*-Fe/TiO_2 films with the Fe compositions of 0, 0.06, 1, and 4%, respectively. The Lorentzian multipeak fitting including the four first-order Raman-active phonon modes ($2B_{1g}$, A_{1g}, and E_g) and a combination mode at about 685 cm^{-1} is required to describe the profile satisfactorily. It suggests that the intensity of B_{1g} phonon mode at about 515 cm^{-1} increase, while that of A_{1g} phonon mode at about 519 cm^{-1} decrease with increasing Fe composition. Corresponding to each Raman-active mode of the anatase phase, there is a scattering tensor α having a distinctive symmetry and the α_{xy} and α_{zz} components relate to the B_{1g} and A_{1g} phonon modes, respectively [x–y belongs to basal (a, b) plane while z is parallel to crystallographic c axis]. It has been verified that the intensities of the B_{1g} and A_{1g} bands could be varied when the growth direction of the samples was rotated around its c axis.[29] It means that the microstructure and surface morphology of the samples are perturbed by the Fe introduction. In addition, the second-order Raman-active mode centered at about 685 cm^{-1} is attributed to a combination of two-phonon scattering process, which is related to the surface morphology and oxygen vacancies. Compared to the Raman spectra of iron oxide, the shoulder structure could not originate from the iron oxide species and the result was confirmed by the XPS reported.[32] The changes of fundamental Raman-active phonon modes and the appearing of the additional vibration mode could be attributed to the Fe introduction, microstructure and surface morphology according to the XRD patterns and AFM images.

3.4 Ellipsometric spectra of the *nc*-Fe/TiO_2 films

SE, based on the reflectance configuration, is an effective tool to extract simultaneously optical constants and thicknesses of

 This journal is © the Owner Societies 2011

Published on 21 June 2011 on http://pubs.rsc.org | doi:10.1039/C0CP02924F
Downloaded by East China Normal University on 25 September 2012

multilayer films. It is a sensitive and non-destructive method that measures relative changes in the amplitude $\Psi(E)$ and phase $\Delta(E)$ of particular directions polarized lights upon oblique reflection from the sample surface.[33,34] Note that the SE parameters $\Psi(E)$ and $\Delta(E)$ are the functions of incident angle, film thickness and optical constants for the material system studied. In order to extract the optical constants and other physical parameters of the anatase Fe/TiO_2 films, the SE spectra were analyzed by a multilayer model with a four-phase layered structure (air/surface rough layer/film/substrate). For wide band gap semiconductor materials, the complex dielectric functions $\tilde{\varepsilon}$ at energies below and above the fundamental band gap can be expressed by the Adachi's model, which is based on the Kramer–Kröning transformation and connected with the electronic band structure. The method reveals the distinct structures at energy of the lowest three-dimensional M_0-type critical point, which is written as $\tilde{\varepsilon}(E) = \varepsilon_\infty + A_0[2 - (1 + \chi_0)^{1/2} - (1 - \chi_0)^{1/2}]/(E_{OBG}^{3/2}\chi_0^2)$. Where, $\chi_0 = (E + i\Gamma)/E_{OBG}$, A_0 and Γ are the strength and broadening values of the E_{OBG} transition, respectively.[35] The Brüggeman effective medium approximation was adopted to calculate the effective dielectric functions of surface rough layer (SRL).[36,37] In the present case, the SRL is described by the assumption of 50% void and 50% Fe/TiO_2. It should be emphasized that the fixed mixture ratio is acceptable because the deviation from the value is very small and can be negligible. As an example, the experimental spectra Ψ and Δ of the anatase Fe/TiO_2 films with the Fe compositions of 0.03 and 2% are shown by the dotted lines in Fig. 6a and b, respectively. The interference patterns due to the thickness of films are observed below the photon energy of 3.6 eV, indicating that the films are transparent in the photon energy region. The dielectric functions of the anatase Fe/TiO_2 films can be extracted by fitting the Adachi's model to the experimental spectra. The fitted model parameter values including the thicknesses of SRL (d_s) and films (d_f) are summarized in Table 2, and the fitted ellipsometric spectra Ψ and Δ are shown by the solid lines in Fig. 6a and b, respectively. As can be seen, a good agreement is obtained between the experimental and fitted spectra in the entirely measured photon energy range.

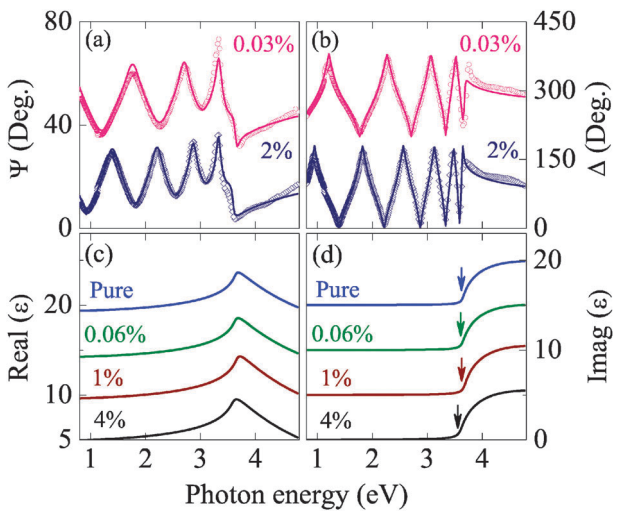

Fig. 6 NIR-UV SE experimental (dotted lines) and best-fitted (solid lines) ellipsometric spectra (a) Ψ and (b) Δ of Fe/TiO_2 films with the Fe compositions of 0.03% and 2%. The evolution of (c) real ε_r and (d) imaginary part ε_i of the dielectric functions for pure and Fe-doped TiO_2 films of 0.06%, 1%, and 4%. The arrows indicate the absorption edge shift's trend. For clarity, Ψ, Δ, Real(ε) and Imag(ε) of the Fe/TiO_2 film are shifted by 30°, 300°, 5, and 5, respectively.

Table 2 The parameter values of the Adachi's dielectric function model for the Fe/TiO_2 films with different Fe compositions determined from the simulation of ellipsometric spectra in Fig. 6

Samples	ε_∞	A_0 ($eV^{3/2}$)	E_{OBG} (eV)	Γ (eV)	d_s (nm)	d_f (nm)
A	0.47	107	3.66	0.03	1	325
B	0.20	112	3.65	0.05	1	274
C	0.27	110	3.64	0.04	2	270
D	0.86	96	3.62	0.02	1	281
E	0.50	112	3.61	0.06	4	230
F	0.25	121	3.62	0.04	1	315
G	0.19	118	3.61	0.03	1	342
H	0.56	119	3.60	0.05	1	335

3.5 NIR-UV dielectric functions and optical band gap

As an example, the real ε_r and imaginary part ε_i of the complex dielectric functions ($\tilde{\varepsilon} = \varepsilon_r + i\varepsilon_i$) of the pure and Fe-doped anatase TiO_2 films of 0.06, 1, and 4% are shown in Fig. 6c and d, respectively. The evaluated dielectric functions with the photon energy are the typical optical response behaviors of semiconductor materials.[34,38] Generally, with increasing the photon energy, ε_r increases and approaches the maximum of about 9.3 at around 3.6 eV, then decreases because of the well-known Van Hove singularities. In the transparent region, ε_i is close to zero and rapidly increases as the photon energy further increases, which indicates that a strong optical absorption appears. It is found that the refractive index n ($n = \mathrm{Real}(\sqrt{\tilde{\varepsilon}})$) in the visible region and the optical band gap E_{OBG} decrease with the Fe composition. In addition, the optical band gap of the anatase Fe/TiO_2 films is about 0.2 eV larger than that of the rutile films fabricated by the same method, which agrees well with the theoretical prediction.[16] The band gap of the present films (~3.6 eV) is larger than that of bulk crystal (3.2 eV). The blueshift can be explained by the surface morphology, structural relaxation, and grain size (*i.e.*, the quantum size effect).[24] For anatase TiO_2, the valence band (VB) is from the O 2*p* level and the conduction band (CB) is from the Ti 3*d* level.[39] The Fe dopant can affect the E_{OBG} by acting as hole traps and by altering the h^+/e^- pair recombination through the processes: $h\nu + Fe^{3+} + h_{VB}^{+} \rightarrow Fe^{4+}$ (hole trap) and $Ti^{4+} + e_{CB}^{-} \rightarrow Ti^{3+} + h\nu$ (electron trap), here the energy level of Fe t_{2g} is just about 0.06 eV above the VB of TiO_2 in this study (see Scheme 2), which is slightly smaller than the value of about 0.1 eV reported.[17] On the other hand, Xing *et al.* reported that the Fe ions in the TiO_2 formed an impurity level under the CB.[40] The introduction of the energy level Fe t_{2g} in the band gap induces the redshift of E_{OBG} varied from 3.66 to 3.60 eV by a charge transfer from the dopant level to the CB or a *d–d* transition in the crystal field. Thus the redshift of E_{OBG} could be due to the dopant composition, d electronic configuration and electron donor composition in the *nc*-Fe/TiO_2 films.

Published on 21 June 2011 on http://pubs.rsc.org | doi:10.1039/C0CP02924F
Downloaded by East China Normal University on 25 September 2012

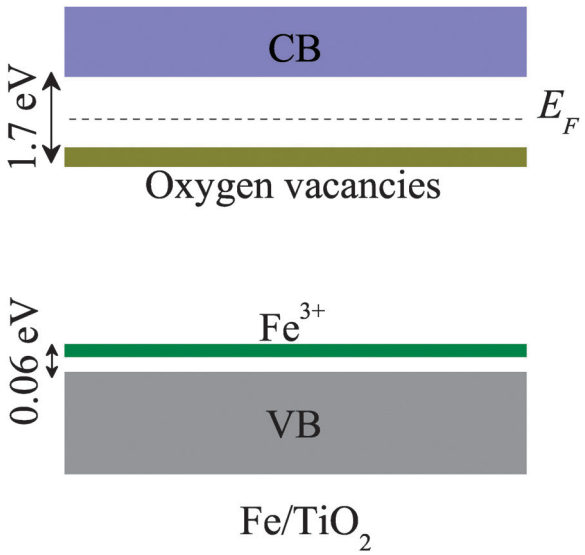

Scheme 2 Schematic representation of the electronic band structure for the anatase Fe-doped TiO_2 films. Note that the Fe dopant energy level and the defect states associated to oxygen vacancies have been shown.

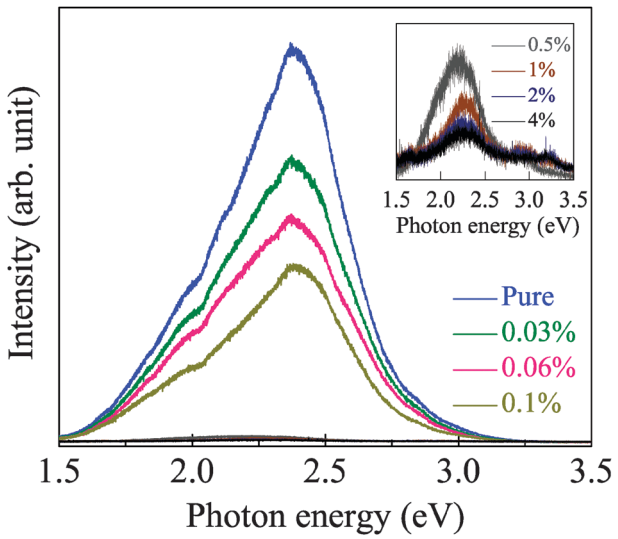

Fig. 7 Composition dependence of room temperature PL emission spectra from the *nc*-Fe/TiO_2 films. The inset shows the enlarged PL emissions of the Fe/TiO_2 films with the Fe compositions of 0.5, 1, 2, and 4%, respectively.

Furthermore, the redshift of E_{OBG} confirms that the Fe element has been indeed incorporated into the TiO_2 host lattice.

3.6 PL emissions of the *nc*-Fe/TiO_2 films

Besides the crystallinity and microstructure, the surface and/or lattice defects (surface states, oxygen vacancies, *etc.*) play an important role in the electronic band structure and photocatalytic activity of the anatase Fe/TiO_2 films.[41] Particularly, PL, which is a non-destructive and high-sensitivity tool, is widely used to study the photophysical and photochemical of semiconductor materials in the photocatalysis and optoelectronics fields. In addition, the PL technique can supply information such as surface/subsurface oxygen vacancies, lattice defects as well as the separation and recombination of photoinduced charge carriers. Fig. 7 shows the room temperature PL emission spectra of the anatase *nc*-Fe/TiO_2 films with different Fe compositions. The inset shows enlarged PL emission lineshapes of the Fe/TiO_2 films with the Fe compositions of 0.5, 1, 2, and 4%, respectively. There are some visible broadening emissions between 1.5 eV and 3.0 eV (410–830 nm) with the maximum at about 2.4 eV. Generally, the intensities of all emission bands approach slowly to the maximum and then decrease quickly to zero with the photon energy due to the lifetime effects originating from the interactions of exciton-phonon, electron-electron, and/or electron-impurity centers. It is found that the peak positions in the PL spectra of the Fe-doped TiO_2 films are in agreement with the undoped one. This means that the presence of Fe element in the TiO_2 host matrix does slightly modify the positions of valence and conduction band edges. Instead, the transition metal induces a new intermediate energy level into the band gap. However, the PL intensity is quite sensitive to the Fe-doped composition. The intensities of the emissions for the Fe/TiO_2 films remarkably decrease with increasing Fe composition. Nagaveni *et al.* argued that the decrease of intensities was attributed to the enhanced metal-metal interaction at a higher composition.[15] On the other hand, we believe that the incorporation of Fe element strongly reduces the oxygen vacancy energy formation, especially at the surface of the anatase Fe/TiO_2 films and generates new oxygen vacancies, which can redistribute the electronic states of films to form a donor state. The oxygen vacancies can trap electrons in the following pathway: $V_O^0 + e_{CB}^- \rightarrow V_O$, *i.e.*, electron trapping in shallow traps. Furthermore, the increment of surface and subsurface oxygen vacancies could capture more photoinduced electrons and reduce their recombination with photoinduced holes, which is an additional channel for the non-radiative relaxation of excited states and would lead to higher photocatalytic activity.[42]

To further investigate the PL properties of the anatase *nc*-Fe/TiO_2 films, low-temperature PL emission spectra of pure TiO_2 and Fe-doped TiO_2 films with the composition of 0.1%, recorded in the temperature range of 9–300 K, are illustrated in Fig. 8a and 9a, respectively. It is obvious that there are some broadening shoulders indicated by the symbol asterisk (*). In order to determine the peak positions of emissions, as Fig. 8b–e and 9b–e show, a five-peak fit of the PL spectra at 9, 100, 200, and 300 K was carried out. The Gaussian multipeak fitting including five peaks and shoulder structure at about 1.9, 2.0, 2.2, 2.4, and 2.6 eV is required to describe the profile satisfactorily. The temperature dependence of peak/shoulder positions in pure and Fe-doped TiO_2 films with the composition of 0.1% are presented in Fig. 8f and 9f, respectively. It indicates that all the bands of Fe/TiO_2 films are shifted towards a higher energy side with the temperature except for the yellow (2.0 eV) and green (2.2 eV) bands. The temperature dependence of peak positions and intensities could be ascribed to the different luminescence mechanisms perturbed by the Fe introduction. In general, PL spectra of anatase TiO_2 material are attributed to several kinds of physical origins: oxygen vacancies,[10,43] self-trapped excitons,[11,44]

 This journal is © the Owner Societies 2011

Published on 21 June 2011 on http://pubs.rsc.org | doi:10.1039/C0CP02924F
Downloaded by East China Normal University on 25 September 2012

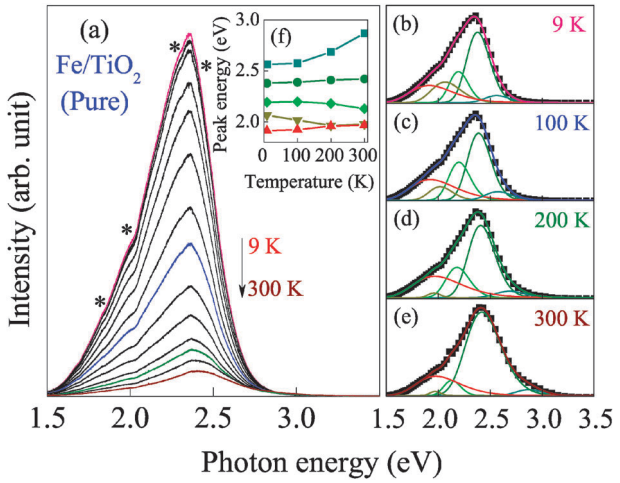

Fig. 8 (a) Low-temperature PL emission spectra of pure TiO_2 film recorded in the temperature range of 9–300 K. A five-peak fit of the PL spectra for the pure TiO_2 film with the temperature of (b) 9 K, (c) 100 K, (d) 200 K, and (e) 300 K. Note that the inset (f) shows the temperature dependence of the corresponding peak/shoulder positions.

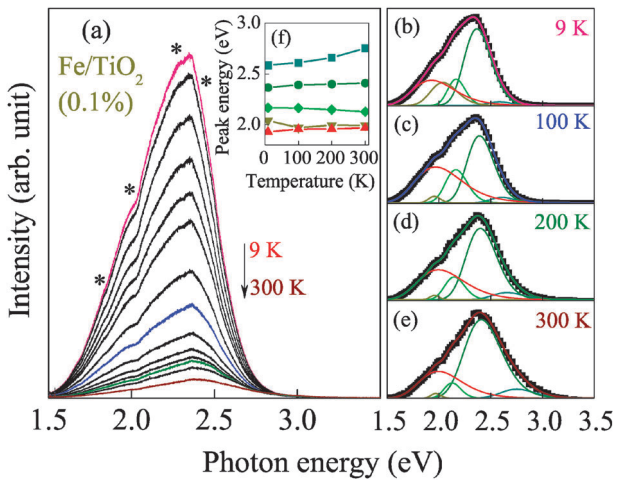

Fig. 9 (a) Low-temperature PL emission spectra of the Fe-doped TiO_2 film (0.1%) recorded in the temperature range of 9–300 K. A five-peak fit of the PL spectra for the Fe-doped TiO_2 film with the temperature of (b) 9 K, (c) 100 K, (d) 200 K, and (e) 300 K. Note that the inset (f) indicates the temperature dependence of the corresponding peak/shoulder positions.

surface states,[15,45] and localized excitons,[46,47] *etc.* It is worth mentioning that the 325 nm line was used as the excitation source with a photon energy of 3.8 eV, which is higher than the optical band gap (3.60–3.66 eV) of the present films. However, no sharp line near the band edge appears, indicating that there are few free exciton emissions because anatase TiO_2 is an indirect band gap material, *i.e.*, the bottom of CB is at Γ point and the top of VB is at M point of the Brillouin zone.[48] Therefore, the charged carriers that occupy those states in the CB and VB can not recombine through the radiative pathway without the phonon assistance due to the conservations of energy and momentum. Such a phonon-assisted recombination process involving a three-body interaction will occur with much lower probability than that in the direct transitions.

Fig. 8f and 9f show that the emission band at about 2.4 eV (517 nm) is the strongest among all the five bands in the investigated temperature range. It can be believed that the large separation of about 1.2 eV between the band gap energy (3.6 eV) and the emission peak energy are ascribed to Stokes shift due to the Franck–Condon effects. Therefore, the emission does not originate from the impurities, oxygen vacancies, and surface states. Such a Stokes shifted emission band can be interpreted as resulting from the fundamental Ti^{4+} to O^{2-} charge transfer transition localized on the TiO_6 octahedron. Moreover, the position of the band holds a constant value with temperature, indicating that this band probably originates from the intrinsic states rather than the surface states. Therefore, it can be reasonable to attribute the green band to the recombination of self-trapped excitons, which arises from strong lattice relaxation. Note that the value of separation is slightly larger than that reported (0.9 eV) because of the different preparation methods and crystalline formation.[23] The weaker shoulder at about 2.6 eV (477 nm) has a remarkable blueshift trend with the temperature, which indicates that the emission could originate from the indirect transition from X_{1a} to Γ_{1b}. Nevertheless, we argued that it associates with Ti–OH reported by some researchers because the Ti–OH bond has induced the occupied states above the VB of about 0.6 eV.[15,24]

Furthermore, surface and subsurface oxygen vacancies or Ti^{3+} states may be formed in the anatase Fe/TiO_2 films and the related PL emission (650 nm) is ascribed to the radiative recombination of excitons trapped to these defects.[49] For the recombination of charge carriers through oxygen vacancies (recombination centers), there are no restrictions from energy and momentum conservation. Therefore, the energy and momentum conservation laws are easily satisfied by the emission of photons. Even if the radiative recombination through defects is forbidden for a certain rule, it would be easier to expend the excess energy in a multistep recombination rather than in a one-step process.[50] Therefore, the position of this PL peak suggests that the energy level of oxygen vacancies is about 1.7 eV below the CB of the anatase Fe/TiO_2 (see Scheme 2). Finally, we can assign the yellow (620 nm) and green (565 nm) bands to the localized excitons because their intensities decrease with increasing the temperature (Fig. 8b–e and 9b–e). It indicates that the emissions could be attributed to the recombination of localized excitons. The low probability that localized excitons decay through non-radiative recombination centers may contribute to the efficient luminescence at low temperature. It has been reported that the disorder introduced by the grain boundaries is responsible for the exciton localization.[46] By connecting the above SE and PL spectra, one can determine the band gap and sub-band levels induced by the Fe doping. As shown in Scheme 2, the Fe^{3+} and oxygen vacancy energy positions in the forbidden band can be uniquely assigned from the band gap of about 3.6 eV. Especially, the Fe dopant energy is determined by comparing the differences of the band gap between the pure and doped TiO_2 films.

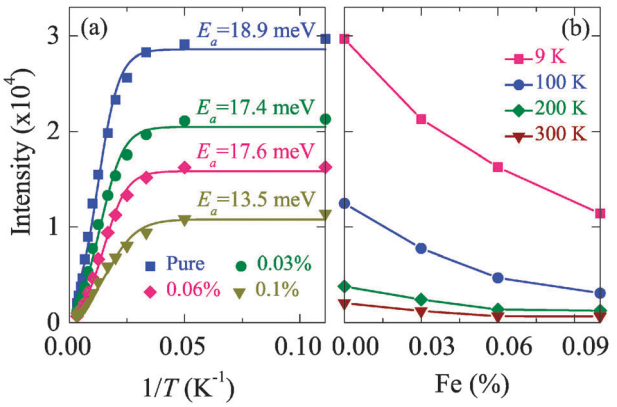

Fig. 10 (a) The PL emission intensity variation of the Fe/TiO_2 films with the compositions of 0, 0.03, 0.06, and 0.1% *versus* $1/T$. The solid lines are the fitting results by eqn (1). (b) Composition dependence of the PL emission intensity for the Fe/TiO_2 films at the temperature of 9, 100, 200, and 300 K.

Fig. 10a shows that all the intensities (dotted lines) of emission bands significantly decrease with increasing the temperature. This phenomenon could be described by the following expression:[46,47]

$$I = \frac{I_0}{1 + a\exp(-E_a/k_B T)}, \quad (1)$$

where $a = \tau_R/\tau_0$ and τ_R is the radiative lifetime of the transition from excited state to ground state, E_a is the activation energy for thermal quenching process, k_B is the Boltzmann's constant, and T is temperature in Kelvin. The best-fitted curves with the solid lines corresponding to the temperature dependence of intensities were shown in Fig. 10a. The value of the parameter E_a is varied from 18.9 to 13.5 meV with increasing Fe composition, which is smaller than that at room temperature ($k_B T_R$ = 25.9 meV). As the temperature increases, the localized excitons could be thermally activated, escape from the ground states, and then transform into the excited state, crystal field, and spin orbit split levels, *etc*. As shown in Fig. 10b, the emission intensity decreases with increasing Fe composition at the temperature point of 9, 100, 200, and 300 K. It indicates that the ratio of radiative and non-radiative of photoelectrons and/or photohole decreases as the function of Fe composition. As we know, the PL efficiency η_R can be calculated by the equation, which is written as[51]

$$\eta_R \equiv \frac{(dN/dt)_{\text{radiative}}}{(dN/dt)_{\text{total}}} = \frac{1}{1 + \tau_R/\tau_{NR}}. \quad (2)$$

Here, N is the number of photons emitted in a given time t, τ_{NR} is the non-radiative lifetime of the transition from excited state to ground state. It suggests that if $\tau_R \ll \tau_{NR}$ then η_R approaches unity ($\eta_R \rightarrow 1$) and the maximum possible amount of light is emitted. On the other hand, if $\tau_R \gg \tau_{NR}$ then η_R is very small ($\eta_R \rightarrow 0$) and the light emission is very inefficient. Thus it is required for the efficient luminescence that the radiative lifetime should be much shorter than the non-radiative lifetime. Therefore, the intensities decrease with the Fe composition because the introduction of Fe could prolong the radiative lifetime and/or shorten the non-radiative lifetime, which may be associated to much rougher surface and lattice defects of the Fe/TiO_2 films. Because the photon energy of the laser line is larger than the band gap of the Fe/TiO_2 films, the UV light penetration depth is about 60 nm. It indicates that the PL and Raman spectra are mainly from the contributions of the surface layer, which is much less than the total film thickness. The PL characteristics can be readily ascribed to the surface and lattice defects, as confirmed by the Raman scattering measurements.

4. Conclusions

High quality anatase *nc*-Fe/TiO_2 films were synthesized by a facile nonhydrolytic sol–gel route. Four fundamental Raman-active phonon modes and an additional vibration at about 685 cm^{-1} are observed from the scattering spectra. The intensity of the B_{1g} phonon mode at 515 cm^{-1} increases, while that of the A_{1g} phonon mode at 519 cm^{-1} decreases with increasing Fe composition. The additional vibration is attributed to a combination of two-phonon scattering process related to the surface morphology and oxygen vacancies. It is verified that the real part of dielectric functions in the transparent region and the optical band gap slightly decrease as a function of Fe composition due to the crystalline structure, grain size, and Fe dopants. The room temperature PL spectra suggest that the emission intensities decrease with increasing Fe compositions since the introduction of Fe could prolong the radiative lifetime and/or shorten the non-radiative lifetime. It is found that the positions of five peaks/shoulders are located at about 1.9, 2.0, 2.2, 2.4, and 2.6 eV, respectively. We can assign these bands to oxygen vacancies (650 nm), localized excitons (620 and 565 nm), self-trapped excitons (517 nm), and indirect transition from X_{1a} to Γ_{1b} (477 nm). In the anatase *nc*-Fe/TiO_2 films, the Fe introduction is considered to be one of the most important factors to affect the surface morphology, lattice vibration, and optical properties such as microstructure, phonon modes, optical constants, optical band gap, and surface and/or lattice defects. The present results could be crucial for future applications of TiO_2-based optoelectronic and photocatalysed semiconductor devices.

Acknowledgements

One of the authors (Jinzhong Zhang) is grateful to Professor Xiaodong Tang, Wenfei Xu, Wenjuan Zhang, Zhenni Zhan, and Zhihua Duan for technical support. This work is financially sponsored in part by Natural Science Foundation of China (Grant Nos. 60906046 and 11074076), Major State Basic Research Development Program of China (Grant Nos. 2007CB924901 and 2011CB922200), Program of New Century Excellent Talents, MOE (Grant No. NCET-08-0192) and PCSIRT, and Shanghai Municipal Commission of Science and Technology Project (Grant Nos. 10DJ1400201, 10SG28 10ZR1409800, and 09ZZ42), and the Program for Professor of Special Appointment (Eastern Scholar) at Shanghai Institutions of Higher Learning.

Published on 21 June 2011 on http://pubs.rsc.org | doi:10.1039/C0CP02924F
Downloaded by East China Normal University on 25 September 2012

This journal is © the Owner Societies 2011

View Online

References

1 H. G. Yang, C. H. Sun, S. Z. Qiao, J. Zou, G. Liu, S. C. Smith, H. M. Cheng and G. Q. Lu, *Nature*, 2008, **453**, 638–641.
2 Y. He, A. Tilocca, O. Dulub, A. Selloni and U. Diebold, *Nat. Mater.*, 2009, **8**, 585–589.
3 J. Virkutyte, B. Baruwati and R. S. Varma, *Nanoscale*, 2010, **2**, 1109–1111.
4 A. M. Asaduzzaman and G. Schreckenbach, *Phys. Chem. Chem. Phys.*, 2010, **12**, 14609–14618.
5 Y. He, O. Dulub, H. Cheng, A. Selloni and U. Diebold, *Phys. Rev. Lett.*, 2009, **102**, 106105.
6 C. Feldmann, *Adv. Mater.*, 2001, **13**, 1301–1303.
7 K. L. Frindell, M. H. Bartl, A. Popitsch and G. D. Stucky, *Angew. Chem., Int. Ed.*, 2002, **41**, 959–962.
8 H. Cheng and A. Selloni, *Phys. Rev. B*, 2009, **79**, 092101.
9 E. Finazzi, C. D. Valentin, G. Pacchioni and A. Selloni, *J. Chem. Phys.*, 2008, **129**, 154113.
10 J. Shi, J. Chen, Z. Feng, T. Chen, Y. Lian, X. Wang and C. Li, *J. Phys. Chem. C*, 2007, **111**, 693–699.
11 Y. Lei, L. D. Zhang, G. W. Meng, G. H. Li, X. Y. Zhang, C. H. Liang, W. Chen and S. X. Wang, *Appl. Phys. Lett.*, 2001, **78**, 1125–1127.
12 Y. Matsumoto, M. Murakami, T. Shono, T. Hasegawa, T. Fukumura, M. Kawasaki, P. Ahmet, T. Chikyow, S.-Y. Koshihara and H. Koinuma, *Science*, 2001, **291**, 854–856.
13 J. Wang, Z. Liu and R. Cai, *Environ. Sci. Technol.*, 2008, **42**, 5759–5764.
14 J. M. D. Coey, M. Venkatesan and C. B. Fitzgerald, *Nat. Mater.*, 2005, **4**, 173–179.
15 K. Nagaveni, M. S. Hegde and G. Madras, *J. Phys. Chem. B*, 2004, **108**, 20204–20212.
16 J. Z. Zhang, Y. D. Shen, Y. W. Li, Z. G. Hu and J. H. Chu, *J. Phys. Chem. C*, 2010, **114**, 15157–15164.
17 C. C. Wang, K. W. Wang and T. P. Perng, *Appl. Phys. Lett.*, 2010, **96**, 143102.
18 W. Choi, A. Termin and M. R. Hoffmann, *J. Phys. Chem.*, 1994, **98**, 13669–13679.
19 J. Zhu, F. Chen, J. Zhang, H. Chen and M. Anpo, *J. Photochem. Photobiol., A*, 2006, **180**, 196–204.
20 Y. Cong, J. Zhang, F. Chen, M. Anpo and D. He, *J. Phys. Chem. C*, 2007, **111**, 10618–10623.
21 K. V. Bineesh, D. K. Kim and D. W. Park, *Nanoscale*, 2010, **2**, 1222–1228.
22 J. L. Gole, S. M. Prokes, O. J. Glembocki, J. Wang, X. Qiu and C. Burda, *Nanoscale*, 2010, **2**, 1134–1140.
23 J. C. Yu, J. Yu, W. Ho, Z. Jiang and L. Zhang, *Chem. Mater.*, 2002, **14**, 3808–3816.
24 A. Iacomino, G. Cantele, D. Ninno, I. Marri and S. Ossicini, *Phys. Rev. B*, 2008, **78**, 075405.
25 M. Mikami, S. Nakamura, O. Kitao and H. Arakawa, *Phys. Rev. B*, 2002, **66**, 155213.
26 M. Kang, *J. Mol. Catal. A: Chem.*, 2003, **197**, 173–183.
27 Y. B. Jiang, W. B. Mi, E. Y. Jiang and H. L. Bai, *J. Vac. Sci. Technol., A*, 2009, **27**, 1172–1177.
28 H. Kamisaka, T. Hitosugi, T. Suenaga, T. Hasegawa and K. Yamashita, *J. Chem. Phys.*, 2009, **131**, 034702.
29 M. Giarola, A. Sanson, F. Monti, G. Mariotto, M. Bettinelli, A. Speghini and G. Salviulo, *Phys. Rev. B*, 2010, **81**, 174305.
30 M. B. Yahia, F. Lemoigno, T. Beuvier, J. S. Filhol, R. P. Mireille, L. Brohan and M. L. Doublet, *J. Chem. Phys.*, 2009, **130**, 204501.
31 J. Zhang, M. Li, Z. Feng, J. Chen and C. Li, *J. Phys. Chem. B*, 2006, **110**, 927–935.
32 I. Chourpa, L. Douziech-Eyrolles, L. Ngaboni-Okassa, J.-F. Fouquenet, S. Cohen-Jonathan, M. Souce, H. Marchais and P. Dubois, *Analyst*, 2005, **130**, 1395–1403.
33 Y. Q. Gao, Z. M. Huang, Y. Hou, J. Wu, Y. J. Ge and J. H. Chu, *Appl. Phys. Lett.*, 2009, **94**, 011106.
34 R. M. A. Azzam and N. M. Bashara, *Eillipsometry and Polarized light*, North-Holland, Amsterdam, The Netherlands, 1977.
35 S. Adachi, *Phys. Rev. B*, 1987, **35**, 7454. 1988, **38**, 12345.
36 D. A. G. Brüggeman, *Ann. Phys. (Leipzig)*, 1935, **24**, 636.
37 H. Fujiwara, J. Koh, P. I. Rovira and R. W. Collins, *Phys. Rev. B*, 2000, **61**, 10832.
38 R. Shirley, M. Kraft and O. R. Inderwildi, *Phys. Rev. B*, 2010, **81**, 075111.
39 Q. Xiang, J. Yu and M. Jaroniec, *Phys. Chem. Chem. Phys.*, 2011, **13**, 4853–4861.
40 M. Xing, Y. Wu, J. Zhang and F. Chen, *Nanoscale*, 2010, **2**, 1233–1239.
41 U. Aschauer, J. Chen and A. Selloni, *Phys. Chem. Chem. Phys.*, 2010, **12**, 12956–12960.
42 A. Roldaán, M. Boronat, A. Corma and F. Illas, *J. Phys. Chem. C*, 2010, **114**, 6511–6517.
43 N. D. Abazović, M. I. Čomor, M. D. Dramićanin, D. J. Jovanović, S. P. Ahrenkiel and J. M. Nedeljković, *J. Phys. Chem. B*, 2006, **110**, 25366–25370.
44 H. Tang, H. Berger, P. E. Schmid and F. Lévy, *Solid State Commun.*, 1994, **92**, 267–271.
45 W. F. Zhang, M. S. Zhang, Z. Yin and Q. Chen, *Appl. Phys. B: Lasers Opt.*, 2000, **70**, 261–265.
46 Z. Xu, H. He, L. Sun, Y. Jin, B. Zhao and Z. Ye, *J. Appl. Phys.*, 2010, **107**, 053524.
47 M. Leroux, N. Grandjean, B. Beaumont, G. Nataf, F. Semond, J. Massies and P. Gibart, *J. Appl. Phys.*, 1999, **86**, 3721–3728.
48 S. B. Ogale, *Adv. Mater.*, 2010, **22**, 3125–3155.
49 L. Cavigli, F. Bogani, A. Vinattieri, V. Faso and G. Baldi, *J. Appl. Phys.*, 2009, **106**, 053516.
50 A. V. Emeline, V. K. Ryabchuk and N. Serpone, *J. Phys. Chem. B*, 2005, **109**, 18515–18521.
51 M. Fox, *Optical Properties of Solids*, Oxford University Press, 2001.

Published on 21 June 2011 on http://pubs.rsc.org | doi:10.1039/C0CP02924F
Downloaded by East China Normal University on 25 September 2012